nature communications

Article

https://doi.org/10.1038/s41467-025-59234-y

Monolithic silicon carbide metasurfaces for engineering arbitrary 3D perfect vector vortex beams

Received: 2 October 2024

Accepted: 9 April 2025

Published online: 29 April 2025

Check for updates

Mingze Liu[1,2,5], Peicheng Lin[1,5], Pengcheng Huo[1,2] ✉, Haocun Qi[3], Renchao Jin[1], Hui Zhang[1], Yongze Ren[1], Maowen Song[1,2], Yan-qing Lu[1,2] ✉ & Ting Xu[1,2,4] ✉

Perfect vector vortex beams (PVVBs) can precisely control the light's polarization and phase along tailored intensity profiles, offering significant potential for advanced applications such as optical trapping and optical encryption. Extending PVVBs from 2D to 3D configurations would provide an additional spatial control dimension and enhance their information capacity. However, a compact and low-loss solution to generating 3D PVVBs remains unresolved. Here, we propose and demonstrate the use of monolithic silicon carbide metasurfaces with polarization-dependent phase-only modulation to engineer arbitrary PVVBs in 3D space. We reconstruct the 3D intensity and polarization distributions of PVVBs along customized trajectories, showing their independence from polarization orders and spherical coordinates on the Poincaré sphere. Additionally, we demonstrate a monolithic metasurface that encodes parallel-channel 3D PVVBs for information encryption. The 3D PVVBs generated from minimalist metasurfaces hold great promise for multidimensional micromanipulation and laser micromachining, high-security information processing and high-dimensional quantum entanglement.

Structured light beams featuring multiple degrees of freedoms, such as wavelength, amplitude, phase and polarization, are widely exploited[1]. By engineering on-demand spatial structures, various complex structured lights, including optical vortex beams (or Laguerre–Gaussian beams), Hermite–Gaussian beams, non-diffracting beams and vectorial beams, have been generated[2], advancing modern optical science and engineering[3]. A typical example of vectorial beams is vector vortex beam (VVB), which carries the total angular momentum of light. The VVB is usually a superposition of two vortices with opposite spin-angular momentum and orbital-angular momentum (OAM) of $l\hbar$, where l is the topological charge[4].

VVBs have been extensively studied and applied in advanced areas such as enhanced imaging, optical tweezers and trapping, optical communications, optical encryption, laser material processing, and quantum information processing[5]. As a significant enhancement, perfect VVBs (PVVBs)[6], as the superposition of two orthogonal circularly polarized perfect vortices, are recently proposed to break the fixed positive correlation of traditional VVBs between their transverse beam size and carrying OAM values. Nevertheless, most of the manipulation of characteristic structures of VVBs are always confined to 2D space, which severely limits concurrent optimization of dimensionality, capacity, and security thresholds in optical encryption[7] and 3D confinement and motion control of particles in optical trapping[8].

[1]National Laboratory of Solid-State Microstructures, College of Engineering and Applied Sciences and Collaborative Innovation Center of Advanced Microstructures, Nanjing University, Nanjing 210093, China. [2]Key Laboratory of Intelligent Optical Sensing and Manipulation, Ministry of Education, Nanjing University, Nanjing 210093, China. [3]School of Electronic Science and Engineering, Nanjing University, Nanjing 210093, China. [4]School of Materials Engineering, Jiangsu University of Technology, Changzhou 213001, China. [5]These authors contributed equally: Mingze Liu, Peicheng Lin.
✉e-mail: huopc@nju.edu.cn; yqlu@nju.edu.cn; xuting@nju.edu.cn

Extending PVVBs from 2D to 3D space would provide an extra spatial control dimension and higher information capacity to advance further science and applications[7–11].

Recently, shaping of optical perfect vortices[12,13] and PVVBs[14] in 3D space has been achieved by computer-generated holography with spatial light modulators (SLMs). However, since SLMs can only handle one fixed incident polarization, this approach requires additional bulky optical components, such as Fourier lenses and other polarization optics, to generate orthogonally polarized optical vortices in separate spatial channels, followed by their coaxial superposition via a grating. These setups complicate the generation process and are prone to optical aberrations caused by misalignment of the cascaded optical elements. In addition, due to large sampling pixels of SLMs used for wavefront control, the generated 3D PVVBs have a relatively low spatial density.

Metasurfaces composed of sub-wavelength structures have been demonstrated to offer a compact and versatile platform for control of multi-dimensional light fields and implementation of novel ultrathin optical components[15–22]. As a powerful advantage, metasurfaces could flexibly tailor the phase or complex-amplitude of different polarization states of incident lights by elaborately designing the arrangement or morphology of micro-nano structures[23], which enables a variety of amazing optical applications via single flat devices[24–33]. Particularly, PVVBs have been achieved in 2D space via various metasurfaces[34–36]. In spite of huge achievements for metasurface-based spatially-structured light, a compact and low-loss solution to generating 3D PVVBs still remains unresolved.

In this work, we aim to utilize monolithic dielectric metasurfaces to demonstrate the generation of arbitrary 3D PVVBs on the hybrid-order Poincaré sphere (HyOPS), featuring 3D customized spatial intensity profiles that are independent of polarization orders and spherical coordinates. We propose a theoretical model of a 3D perfect vortex with a customized curve modulated by the Dirac function and explore its metasurface-based approximate generation scheme using a phase-only modulation method. Through composite phase control, we demonstrate that monolithic silicon carbide (SiC) metasurfaces can directly achieve the coaxial superposition of two orthogonally circularly polarized 3D perfect vortices without the need for additional optical elements, enabling the creation of arbitrary 3D PVVBs with nearly identical spatial trajectories but different polarization orders. Additionally, by exploiting the multiple degrees of freedom of a 3D PVVB, we demonstrate an optical information encryption scheme for enhanced information security, using a minimalist metasurface to encode a series of 3D PVVBs in spatially separated parallel channels.

Results

Principle of generating 3D PVVBs via monolithic phase-only metasurfaces

Figure 1a exhibits the schematic of a monolithic metasurface for the generation of various 3D PVVBs with customized 3D intensity trajectories and polarization orders in spatially separated parallel channels. A 3D PVVB represented by a HyPOS can be expressed as the linear superposition of a pair of orthogonal polarization basis, e.g., two orthogonal circular polarization 3D perfect vortices carrying different topological charges, with varying complex coefficients of $a_R e^{ib_R}$ and $a_L e^{ib_L}$. The complex amplitude of a 3D PVVB can be expressed by:

$$|\boldsymbol{E}_{3\mathrm{D-PVVB}}\rangle = a_R e^{ib_R}|\boldsymbol{E}_{3D\,PV-R}, l_M\rangle + a_L e^{ib_L}|\boldsymbol{E}_{3D\,PV-L}, l_N\rangle \quad (1)$$

where $|\boldsymbol{E}_{3D\,PV-R}, l_M\rangle$ and $|\boldsymbol{E}_{3D\,PV-L}, l_N\rangle$ are the complex amplitudes of right and left circularly polarized (RCP and LCP) 3D perfect vortices with topological charges of l_M and l_N, respectively. a_R, a_L, b_R and b_L are the amplitudes and phases of the RCP and LCP 3D perfect vortices, respectively. The polarization order l_p of the 3D PVVB equals $(l_M + l_N)/2$.

To achieve a 3D PVVB, we first consider a theoretical model of a 3D perfect vortex with the topological charge of l and a customized 3D intensity trajectory composed of a series of disjoint light points. Here, the complex amplitude of a RCP or LCP 3D perfect optical vortex, modulated by the Dirac function, can be defined as:

$$|\boldsymbol{E}_{3D\,PV}, l\rangle = \sum_n \delta[\rho - \rho_0(t_n)]\,\delta[z - z_0(t_n)]e^{il\varphi}\begin{bmatrix}1\\ \pm i\end{bmatrix} \quad (2)$$

where $\rho_0(t_n)$ and $z_0(t_n)$ are the parametric coordinates of a 3D's closed trajectory, $t_n = \varphi$, and n is the number of discrete light points. To generate the light field expressed by Eq. (2), one can use the Fresnel diffraction integral to calculate the field distribution in the initial (aperture) plane at $z = 0$. The complex amplitude of the required initial scalar field is approximatively derived as: $\boldsymbol{E}_{in}(r,\theta) \propto \sum_n J_l[k_{r0}(t_n)r]e^{-ik[r^2+\rho_0(t_n)^2]/[2z_0(t_n)]}e^{il\theta}$ (see details in supplementary Section S1). $k = 2\pi/\lambda$, and J_l is a l-order Bessel function of the first kind with a parametric radial wavevector of $k_{r0}(t_n) = k\rho_0(t_n)/z_0(t_n)$. The light field expressed by the function J_l can be approximatively created by using a deformed axicon phase element with a phase profile of $k_{r0}(t_n)r$. According to $\boldsymbol{E}_{in}(r,\theta)$, it is possible to generate a 3D perfect vortex by utilizing a pure-phase optical element to encode a superposed phase profile of $\varphi_{\mathrm{total}} = \varphi_{\mathrm{dfd\text{-}axicon}} + \varphi_{\mathrm{dfd\text{-}lens}} + \varphi_{\mathrm{sprial}}$. These phase profiles are given by:

$$\varphi_{\mathrm{dfd\text{-}axicon}}(r, t_n) = -k\rho_0(t_n)r/z_0(t_n) \quad (3)$$

$$\varphi_{\mathrm{dfd\text{-}lens}}(r, t_n) = -k[r^2 + \rho_0(t_n)^2]/[2z_0(t_n)] \quad (4)$$

$$\varphi_{\mathrm{sprial}}(\theta) = l\theta \quad (5)$$

Here, the 3D closed rounded polygonal curve in this work are given by $\rho_0(t_n) = r_0(1 - s\cos pt_n)$ and $z_0(t_n) = f_0(1 - u\sin vt_n)$. This curve can be regarded as a 3D stretching deformation of a 2D circle with a radius of r_0 at a distance of f_0 in space. The parameters s and p control the corner smoothness and the number of sides for the polygonal curve, respectively; the parameters u and v control the longitudinal height and the times of fluctuations in the polygonal curve, respectively. For given an initial light field of $e^{i\varphi_{\mathrm{total}}}$ at $z = 0$, we numerically analyze its diffracted light field at a certain propagation distance by using Fresnel diffraction integral. As a simple example, the simulated transverse intensity and phase distributions of different perfect vortices with topological charges of $l = 1$, 20 and 30 in 3D space are shown in supplementary Fig. S1. The transverse intensity profiles of these perfect vortices are nearly identical at the same z propagation distances, demonstrating their perfect properties that the beam sizes are nominally independent of their topological charges. Therefore, thanks to the free adjustment of the light intensity and helical phase distribution in 3D spatial structure for the perfect vortex, any 3D PVVB with customized intensity trajectory and arbitrary polarization order can be constructed on a HyOPS via the linear superposition of RCP and LCP 3D perfect vortices carrying different topological charges.

To create 3D PVVB in a highly efficient and integrated manner, a monolithic dielectric metasurface is used to provide two distinct spin-dependent phase profiles $\varphi_{\mathrm{total,RCP}}$ and $\varphi_{\mathrm{total,LCP}}$ (Fig. 1b) of different topological charges l_M and l_N, without additional amplitude modulation and other optical elements. This polarization-multiplexed metasurface would enable the simultaneous generation and coaxial superposition of arbitrary RCP and LCP 3D perfect vortices, free of theoretical energy loss. Based on the synchronous modulation principle of propagation and geometric phase, a series of meta-atoms with varying in-plane dimensions is required to act as subwavelength half-

https://doi.org/10.1038/s41467-025-59234-y

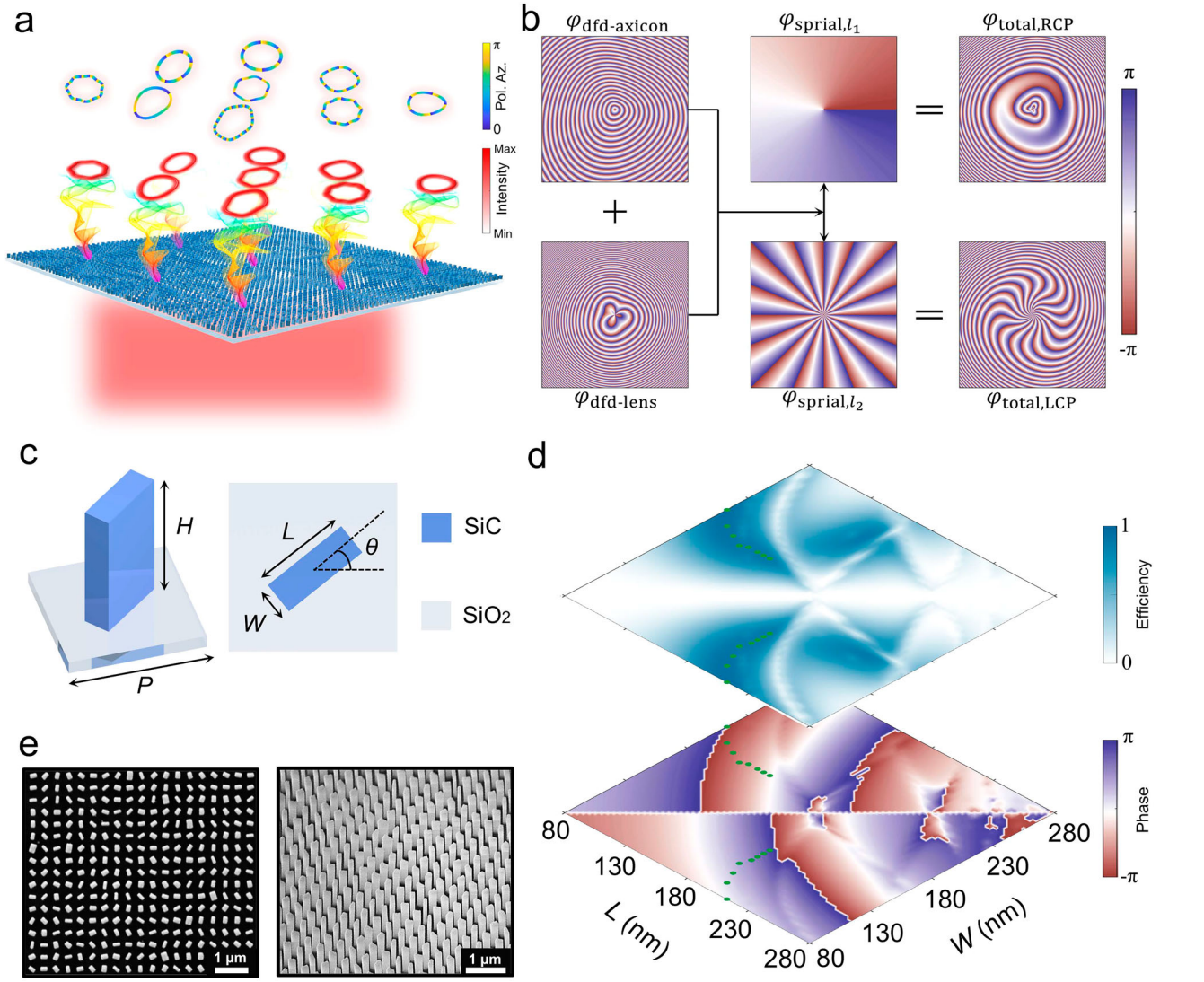

Fig. 1 | Design principle of the metasurface-based arbitrary 3D perfect vector vortex beams (PVVBs). a Schematic of the generation of 3D PVVBs with customized 3D intensity trajectories and arbitrary polarization orders in spatially separated parallel channels via a monolithic metasurface. **b** The two spin-dependent phase profiles imparted by the metasurface for generating two RCP and LCP 3D perfect vortices with different topological charges. **c** Schematic of the meta-atom of the metasurface. **d** The intensity (top) and phase (bottom) of the simulated complex cross-polarization transmission coefficients for the 6561 SiC nanopillars. The green dots indicate the location of 16 selected SiC nanopillars. **e** The SEM images of nanopillar arrays of a fabricated SiC metasurface.

wave plates with high transmission efficiencies over a full 2π phase coverage at the operating wavelength and arranged at specific spatial rotation angles to construct the metasurface, completely decoupling the two different phase profiles of incident orthogonal circular polarizations. As illustrated in Fig. 1c, the meta-atom of the metasurface is composed of a rectangular SiC nanopillar with a fixed height H of 1000 nm arranged on a silica substrate with a square lattice period P of 380 nm. Here a group of 6561 SiC nanopillars with varying lengths (L) and widths (W) ranging from 80 nm to 280 nm is numerically simulated via the finite-difference time domain algorithm (see details in Methods). Figure 1d shows the intensity (top) and phase (bottom) of the simulated complex cross-polarization transmission coefficients for the above SiC nanopillars. A set of 16 SiC nanopillars (denoted by green dots) are selected to cover a full 2π phase range and exhibit high cross-polarization conversion efficiency (PCE) at the operation wavelength of 630 nm. The average cross-PCE and co-PCE of these selected SiC nanopillars are 90.82% and 0.09%, respectively, which ensures the generation efficiency of these vortices. We fabricate two SiC metasurface devices for the generation of different 3D PVVBs by using a method compatible with the semiconductor process. This process mainly includes the plasma enhanced chemical vapor deposition of SiC thin films, the electron beam lithography (EBL) for patterning metasurface arrays and the inductively coupled plasma (ICP) reactive ion etching of SiC nanopillar arrays (see details in Methods). Figure 1e shows scanning electron micrographs (SEM) of nanopillar arrays of the fabricated SiC metasurface.

Experimental demonstration of 3D PVVBs

We design and fabricate two monolithic polarization-multiplexed SiC metasurfaces to create two 3D PVVBs (PVVB1 and PVVB2) along a customized 3D curve with the parameters of $s = 1/20$, $p = 2$, $u = 7.5$ and $v = 1$. PVVB1, with polarization order $l_p = +5$, is the superposition of RCP perfect vortex 1 with $l_1 = +15$ and LCP perfect vortex 2 with $l_2 = +5$; while PVVB2, with polarization order $l_p = -15.5$, is the superposition of RCP perfect vortex 3 with $l_3 = -23$ and LCP perfect vortex 4 with $l_4 = +8$. Both metasurfaces share the same parameters: $r_0 = 60$ μm and $f_0 = 300$ μm.

We first characterize two pairs of RCP and LCP 3D perfect vortices generated by the two SiC metasurfaces by using an experimental setup shown in supplementary Fig. S2. We capture 201 transverse intensity

https://doi.org/10.1038/s41467-025-59234-y

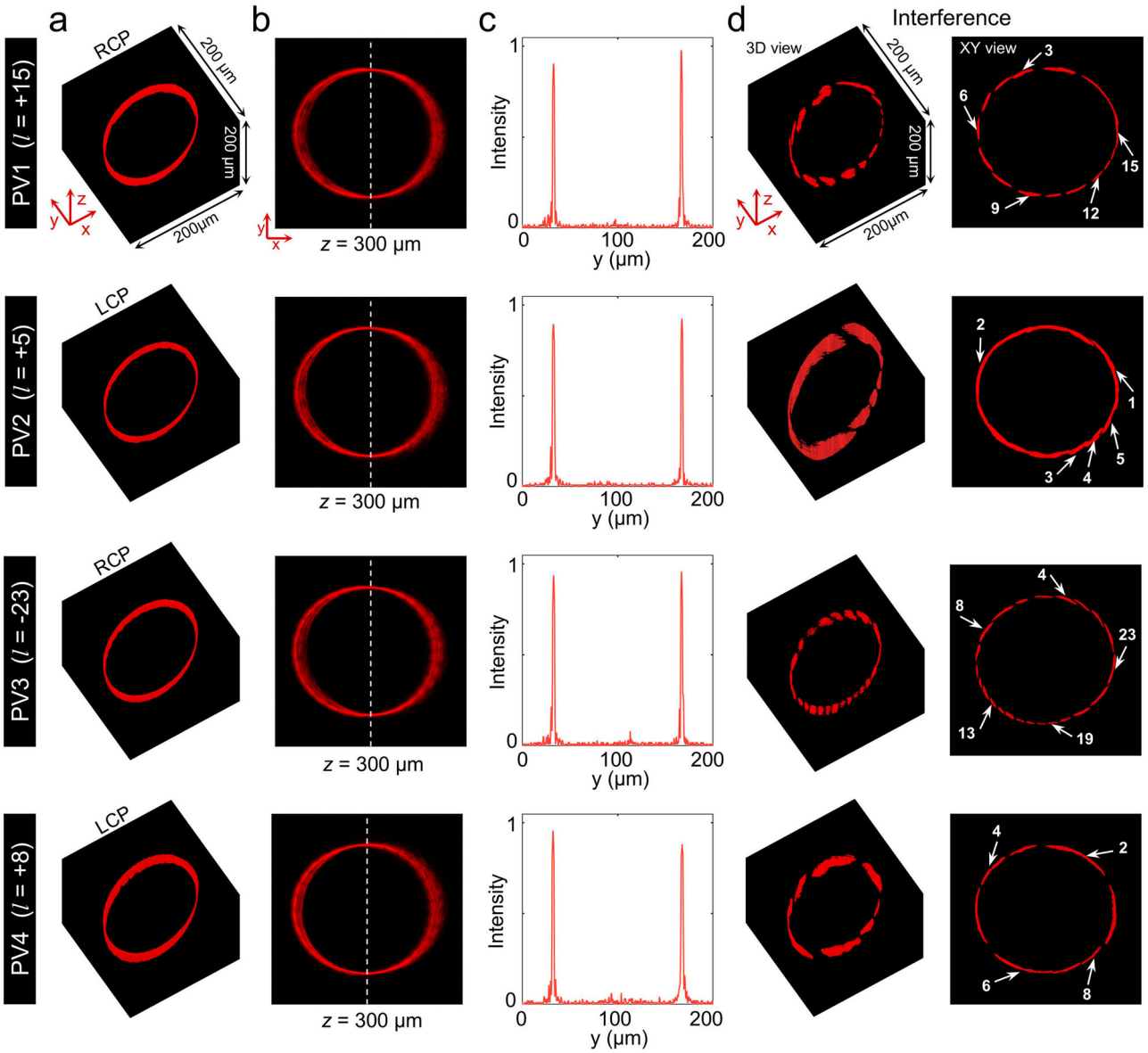

Fig. 2 | Experimental generation of RCP and LCP 3D perfect vortices based on monolithic SiC metasurfaces. a The measured and reconstructed 3D light fields of two pairs of generated 3D perfect vortices including RCP 3D perfect vortex 1 with l of +15, LCP 3D perfect vortex 2 with l of +5, RCP 3D perfect vortex 3 with l of −23, LCP 3D perfect vortex 4 with l of +8, respectively. For simplicity, perfect vortex 1 to perfect 4 in the figure are labeled as "PV1" to "PV4". **b**, **c** The measured transverse intensity images of four 3D perfect vortices at $z = 300$ μm and their cross sections along the white dashed lines. **d** The measured 3D interference patterns corresponding to the four 3D perfect vortices in (**a**).

images of each 3D perfect vortex at 2 μm intervals along the z direction, ranging from $z = 0$ μm (*i.e.*, the surface of the metasurface) to $z = 400$ μm. The 3D light fields of the four 3D perfect vortices reconstructed from these image sequences are shown in Fig. 2a. The 3D contours of these perfect vortices appear very similar. Additionally, we quantitatively compare the sizes of the x-y plane intensity distributions (Fig. 2b) of the four 3D perfect vortices at $z = 300$ μm and the cross sections of these in-plane intensity images along the white dashed lines are shown in Fig. 2c. A size growth factor η of two orthogonally polarized perfect vortices with topological charges of l_M and l_N is defined as: $\eta = (d_{l_M} - d_{l_N})/d_{l_N}$, where $|l_N| < |l_M|$, and d is the distance between the two points with the highest intensity on the white dashed line path, representing the size of optical beams along a certain direction. The distance d in the y direction is measured as, for SiC metasurface 1: 134.51 μm for perfect vortex 1 with $l_1 = +15$, 132.63 μm for perfect vortex 2 with $l_2 = +5$; for SiC metasurface 2: 134.95 μm for perfect vortex 3 with $l_3 = -23$, and 133.85 μm for perfect vortex 4 with $l_4 = +8$, respectively. The size growth factor η is calculated as: 1.42% for perfect vortex 1 and perfect vortex 2, and 0.82% for perfect vortex 3 and perfect vortex 4. To determine their topological charge numbers, we measure the 3D light fields of the interference patterns for the four generated 3D perfect vortices by using a setup shown in supplementary Fig. S3. The corresponding 3D views of these reconstructed interference patterns and their projections on the x-y plane (labelled XY view) are presented in Fig. 2d. The numbers of petals of the four interference patterns are 15 for perfect vortex 1, 5 for perfect vortex 2, 23 for perfect vortex 3, and 8 for perfect vortex 4, corresponding to the absolute values of their topological charges l of 15, 5, 23, and 8, respectively. The petal arrangement direction of perfect vortex 3 is opposite to that of the other three perfect vortices, indicating that its topological charge has the opposite sign compared to the others. These experimental results show that the sizes of the 3D perfect

https://doi.org/10.1038/s41467-025-59234-y

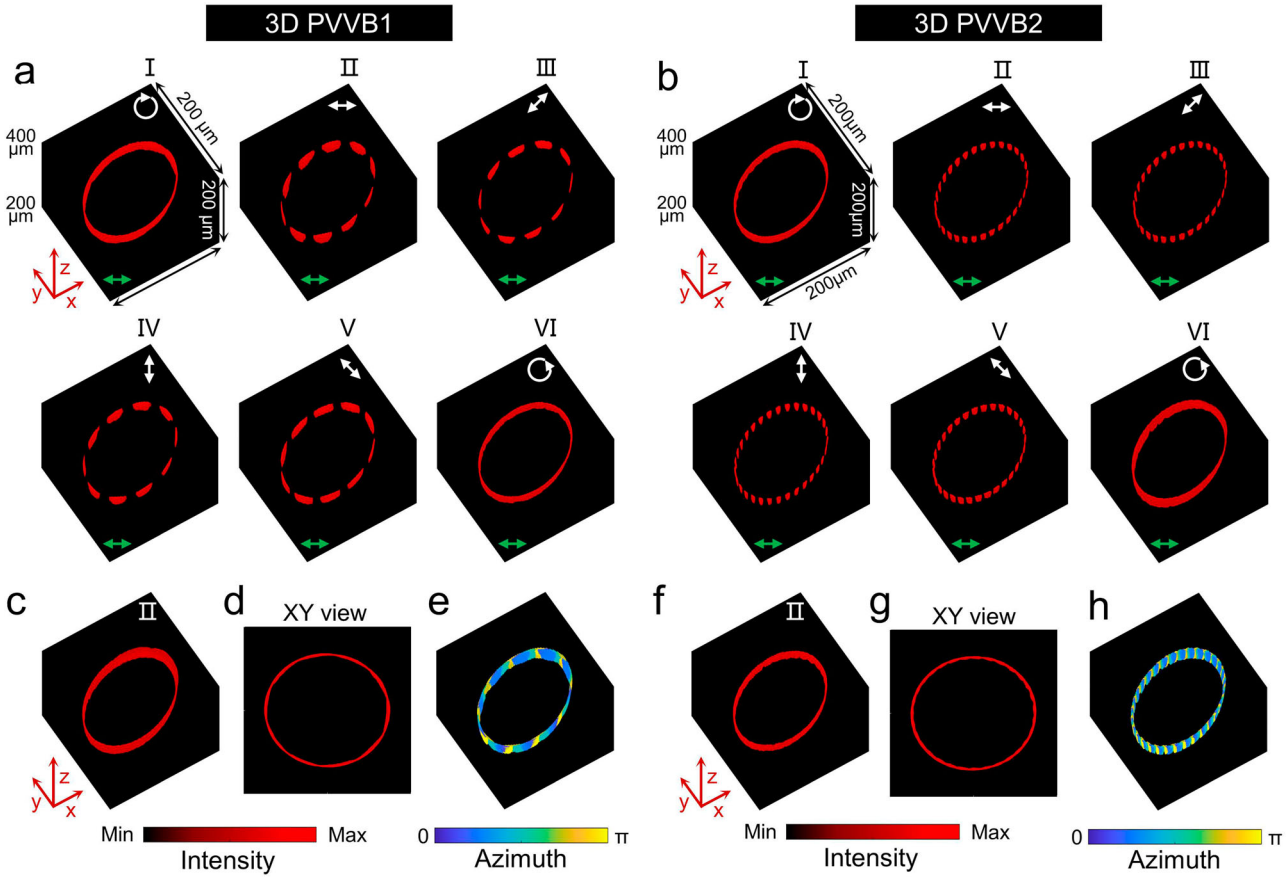

Fig. 3 | Experimental demonstration of 3D PVVBs with customized intensity trajectories. a, **b** The measured and reconstructed 3D spatial intensity distributions of 6 states for the two 3D PVVBs (namely PVVB1 and PVVB2) with polarization orders l_p of +5 and −15.5 after filtering through a horizontal linear polarizer (denoted by green arrows). These output states, I to VI, are generated by illuminating metasurfaces with RCP, four linearly polarized, and LCP states of lights (denoted by white arrows). **c**, **f** The measured and reconstructed 3D spatial intensity distributions of the state II for the PVVB1 and PVVB2 without any polarization analyzer. **d**, **g** The projections of the 3D spatial intensity distributions in (**c**, **f**) on the x-y plane. **e**, **h** The measured and reconstructed 3D distributions of polarization azimuth of the state II for the PVVB1 and PVVB2. The polarization orientation parallel to the *x*-axis is defined as 0 or π rad.

vortices generated by our method exhibit minimal change with increasing topological charge, suggesting that the customized intensity trajectories are largely independent of the vortices' topological charges.

By adjusting the polarization state of the light incident on the fabricated metasurfaces, we can achieve controlled generation of various states of the 3D PVVBs. Here, six incident polarization states, including RCP, LCP and four linearly polarized states, are selected, and their corresponding coordinates (denoted by green dots) are displayed on the HyOPS in supplementary Fig. S4. To exhibit their 3D light fields, we experimentally capture a series of transverse intensity distributions of various states for the generated 3D PVVBs at 2 μm intervals along the light propagation direction. Figure 3a, b show the reconstructed 3D intensity profiles of the states I to VI after filtering through a horizontal linear polarizer (denoted by green arrows) for PVVB1 and PVVB2, respectively. As expected, the measured intensities of the states II to V exhibit 3D petal-like patterns with $2|l_p|$ lobes, i.e., 10 lobes for PVVB1 (l_p = +5) and 31 lobes for PVVB2 (l_p = -15.5), which arises from the azimuth distributions of their spatially anisotropic linear polarization along the customized 3D trajectories. Furthermore, the 3D light fields of the state II of PVVB1 and PVVB2 are reconstructed from the corresponding image sequences captured without any polarization analyzers, as shown in Fig. 3c, f. The XY views of reconstructed 3D intensity profiles for PVVB1 and PVVB2 are also presented in Fig. 3d, g. We observe that the slanted, continuous elliptical intensity profiles of the generated 3D PVVBs with different polarization orders exhibit highly similar contours. The *x*-*y* plane intensity profiles at z = 300 μm and their cross sections along the *y* direction are shown in Fig. S5, with the measured distances d being 134.4 μm for PVVB1 and 134.4 μm for PVVB2, which are close to theoretical values of 133.0 μm.

Moreover, the 3D spatial distributions of the polarization azimuth for state II of both PVVB1 and PVVB2 are quantitatively measured using Stokes polarimetry, as shown in Fig. 3e, h. It can be seen that the linear polarization orientations rotate by rotate +10π and -31π per round trip in the clockwise direction for PVVB1 and PVVB2, respectively. The average cross-polarization conversion efficiencies of the two polarization-multiplexed metasurfaces are measured as 65.91% for RCP to LCP, and 65.37% for LCP to RCP, respectively (see details in Methods). These results demonstrate that the proposed monolithic SiC metasurfaces can generate arbitrary PVVBs with 3D intensity trajectories, independent of their topological charges or polarization orders.

Optical information encryption using 3D PVVBs

The metasurface-based 3D PVVB can offer a compact, low-loss and high-capacity platform to advance optical information security technology. A variety of distinct 3D PVVBs featuring multiple parameters could be used as different information carriers for optical encoding. As a simple example of demonstration, a series of 3D PVVBs, characterized by three geometrical parameters v, r_0, p and a polarization order l_p, are chosen to encode different 8-digit binary numerals. Specially, the four parameters−v with 2 values, r_0 with 2

https://doi.org/10.1038/s41467-025-59234-y

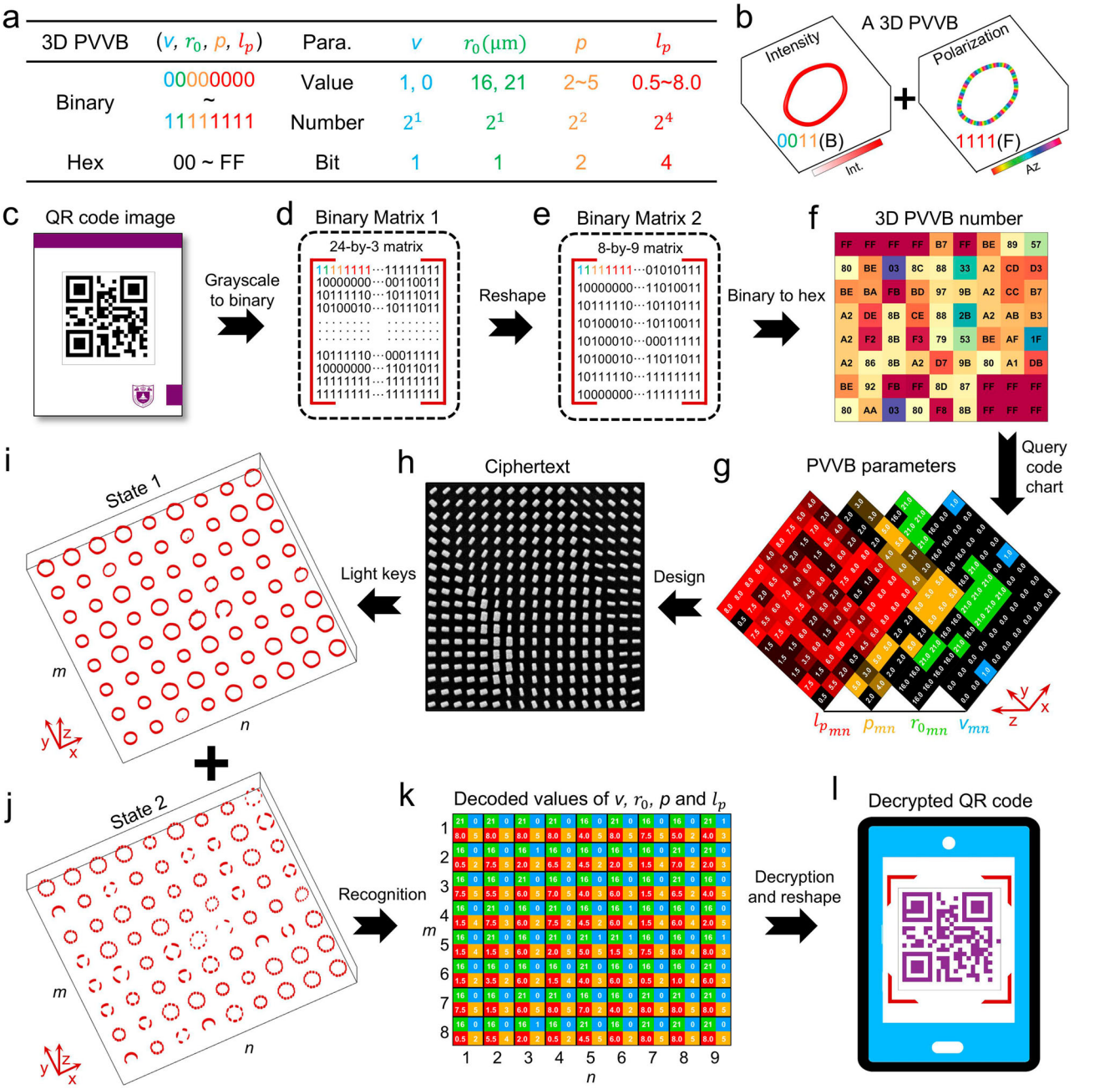

Fig. 4 | Deign principle and experimental demonstration of optical encoding and image encryption using a metasurface-based 3D PVVB array. a A series of 3D PVVBs, characterized by four parameters v, r_0, p, and l_p, represent a group of 8-digit binary numerals, from 00000000 to 11111111 (corresponding to the hexadecimal numerals from 00 to FF). v, r_0, p and l_p denote the first digit (blue), the second digit (green), the third to fourth digits (yellow), and the fifth to eighth digits (red) of an 8-digit binary numeral, respectively. **b** shows an example of the intensity and polarization distribution of a 3D PVVB with $v = 1$, $r_0 = 16$ μm, $p = 5$ and $l_p = 8.0$, denoting a binary numeral "00111111" (or a hexadecimal numeral "BF"). **c** The image of the generated QR code with 24 × 24 black and white blocks. **d** A 24-by-3 binary matrix transformed from the QR code. **e** An 8-by-9 binary matrix reshaped from (**d**). **f** An 8-by-9 array of hexadecimal serial numbers of required 3D PVVBs. **g** The values of four parameters for the 3D PVVB array. **h** The SEM image of a portion of the fabricated metasurface ciphertext. **i, j** The two measured and reconstructed 3D light fields (namely State 1 and State 2) of the 3D PVVB array by using RCP and x-polarized states of incident lights. **k** The identified values of v, r_0, p, and l_p for the generated 3D PVVB array. v, r_0, p and l_p of each PVVB are labeled by the square blue, green, yellow and red background. **l** The decrypted image of the QR code.

values, p with 4 values, and l_p with 16 values—are set to denote the first digit, the second digit, the third to fourth digits, and the fifth to eighth digits of an 8-digit binary numeral, respectively. As such, the binary numerals from 00000000 to 11111111 (corresponding to the hexadecimal numerals from 00 to FF) can be represented by 256 different kinds of 3D PVVBs (Fig. 4a). The value ranges and the number of possible values for the four parameters are also shown in Fig. 4a. A code chart related to the hexadecimal serial numbers of 3D PVVBs and corresponding beam parameters is constructed and shown in supplementary Table S1. For instance, Fig. 4b shows the intensity and polarization distribution of a 3D PVVB with $v = 1$, $r_0 = 16$ μm, $p = 5$ and $l_p = 8.0$. It features a 3D rounded pentagon intensity trajectory with a smaller outer profile and its linear polarization orientations rotate 16π rad per round trip in the clockwise direction. We can know that it denotes a binary numeral "00111111" (or a hexadecimal numeral "BF") according to the code chart.

As a proof of concept, we demonstrate an information encryption scheme for optical anti-counterfeiting by using metasurface-generated 3D PVVBs. QR code is a widely used two-dimensional matrix barcode that stores data information. As an encrypted image, a 2D QR code with 24 × 24 black and white blocks (Fig. 4c) is transformed into a 24 × 24 binary matrix where each element, based on the block color, is either 0 or 1. Grouping every eight elements from each row into 8-digit binary numbers, the 24 × 24 matrix is condensed into a 24 × 3 binary matrix (Fig. 4d), and reshaped into an 8 × 9 binary matrix (Fig. 4e) for facilitating subsequent metasurface fabrication and characterization. This matrix is then converted into a hexadecimal matrix, where each 2-digit numeral represents the serial numbers of the required 3D PVVBs (Fig. 4f). By referencing the code chart, the user obtains four parameters of the 3D PVVB array (Fig. 4g) and calculates the RCP and LCP phase profiles. A SiC metasurface, termed ciphertext (Fig. 4h), is designed and fabricated based on these phase profiles, encoding the QR code image onto this minimalist device.

To decode the message, RCP and x-polarized light are incident onto the metasurface ciphertext, and two 3D optical fields, corresponding to two states of the 3D PVVB array (State 1 and State 2), are captured after filtering through an LCP analyzer and a y-direction linear polarizer, as reconstructed in Fig. 4i, j. Projections of these states onto the x-y plane are also shown in supplementary Fig. S6. From State 1, by analyzing the height along the z-direction, the maximum outer ring size, and the annular shape on the x-y plane, the values of υ, r_0, and p can be identified. For State 2, by counting the number of lobes, N, in the petal-like intensity pattern, the value of l_p can be determined as $N/2$. For instance, a 3D PVVB in the first row and ninth column of State 1 has a height of ~18 μm in the z-direction, a maximum outer diameter of ~42 μm, and a rounded triangular ring shape, with the corresponding values of υ, r_0, and p recognized as 1, 21 μm, and 3, respectively. The intensity pattern of the 3D PVVB at the same position in State 2 has eight petals, indicating $l_p = 4.0$. In this way, the four parameters of the entire 3D PVVB array are determined and displayed in Fig. 4k, where υ, r_0, p, and l_p of each PVVB are labeled with blue, green, yellow, and red backgrounds, respectively. The hexadecimal serial number of the 3D PVVB in the first row and ninth column of the array is recognized as "57" by querying the code chart, and the decoded number of the entire 3D PVVB array is shown in supplementary Fig. S7. By sequentially converting this hexadecimal matrix into a binary matrix, reshaping it into a 24 × 3 matrix, and splitting each 8-digit binary numeral into single-digit elements, a 24 × 24 binary matrix is decrypted. Finally, this matrix can be transformed into the original 2D QR code (Fig. 4l).

Discussion

In this work, we have experimentally demonstrated a compact and low-loss platform for achieving generalized 3D PVVBs by utilizing monolithic SiC metasurfaces with phase-only modulation. This minimalist platform enables the customization of annular intensity trajectories in 3D space for PVVBs, including their heights, shapes, and sizes, which remain nominally independent of topological charges and polarization orders, respectively. Leveraging this "perfect" property, we experimentally implement an image encryption scheme for optical anti-counterfeiting by using a metasurface-encoded 3D PVVB array to represent different numerical symbols. This work extends the engineering of beam characteristics for the metasurface-based perfect vortices and PVVBs from a 2D plane to 3D space, providing an additional dimension of spatial control and higher information capacity for applications, such as 3D manipulation of micro-nano particles, higher-security information processing and high-dimensional quantum entanglement.

Compared with some OAM/VVB-based encryptions[37–39], the 3D PVVB allows for high-dimensional encoding and the additional degree of freedom in the 3D structure (e.g., height, shape, and polarization distribution along the z-axis) provides an extra layer of complexity, making it more challenging to decode or replicate the beam without precise knowledge of its parameters. The 3D PVVB-based encryption uses a non-interferometric system, which makes the decoding process simple and less susceptible to environmental perturbations and mechanical vibrations. Additionally, the 3D PVVB holds significant promise for 3D optical trapping applications[7,40]. It would enable precise regulation of particle speed and facilitates advanced control mechanisms, such as halting or reversing their motion at will, along customizable 3D trajectories.

Methods

Numerical simulation of meta-atoms

The linearly birefringent meta-atom, composed of a SiC rectangular nanopillar and a silica square substrate with a lattice period P of 380 nm, are simulated by using the finite-difference time domain method. Considering the capability of actual micro-nano processing technology, the heights of SiC nanopillars are set to 1000 nm. The lengths (L) and widths (W) of SiC nanopillars range from 80 nm to 280 nm with a sweep interval of 2.5 nm. Periodic boundary conditions are applied along the x and y axes, while a perfectly matched layer boundary condition is used in the z direction. The used complex refractive index of SiC is shown in supplementary Fig. S8. The plane wave illumination with x and y polarization are sequentially applied from the substrate side, and the transmission efficiencies (T_x and T_y) and phase shifts (Φ_x and Φ_y) of 6561 meta-atoms are obtained for x- and y- polarized light with a wavelength of 630 nm, respectively (supplementary Fig. S9). The cross- and co- PCE are calculated as: $|0.5(t_x e^{i\Phi_x} - t_y e^{i\Phi_y})|^2$ and $|0.5(t_x e^{i\Phi_x} + t_y e^{i\Phi_y})|^2$, respectively, where $t_{x/y} = \sqrt{T_{x/y}}$. The cross-PCE of these meta-atoms are calculated and shown in the top panel of Fig. 1d.

Fabrication of the SiC metasurfaces

The fabrication process of SiC metasurfaces is summarized as follows. By using plasma enhanced chemical vapor deposition, a layer of SiC film with a thickness of 1000 nm is clothed on a 500 μm-thick fused silica substrate. Then, a layer of hexamethyldisilazane is vapor-coated on the SiC film to enhance adhesion. A layer of 200 nm-thick positive electron beam resist and a thin layer of water-soluble conductive adhesive are spin-coated on the samples successively, where the conductive adhesive is used to mitigate the charging effect during later electron beam exposure. Next, the nanopatterns are defined in the resist by using EBL with an accelerating voltage of 125 kV and a beam current of 1 nA, followed by the development in a solution of o-Xylene. A layer of 30-nm-thick aluminum is than physically vapor-deposited on the sample by using an electron beam evaporator. A lift-off process is done by soaking the sample in n-methyl-pyrrolidone for 10 min at 80 °C, coupled with subsequent gently ultrasonic cleaning. This step leads to patterns reversion from the resist to the aluminum hard mask. Whereafter, the ICP reactive ion etching is implemented via an optimized anisotropic etching recipe, in which the chamber pressure is controlled at 13.5 mTorr, the ICP generator RF power is 500 W, the bias RF power is 40 W, and the ratio of C_4F_8/SF_6 is tuned to be 8/3. Finally, the metasurfaces composed of SiC nanopillars are obtained after removing the residual aluminum with the stripping solution.

Measurement of cross-polarization conversion efficiency of metasurfaces

We first illuminate the RCP or LCP light on the metasurface samples, and use an objective lens and visible detector to capture their transmission light intensity distributions of the sample surfaces, marked as

an m-by-n matrix I^{o1} or I^{o2} through an LCP or RCP analyzer. Second, we remove the metaurface samples and measure the intensity distributions of incident RCP or LCP light (marked as an m-by-n matrix I^{in1} or I^{in2}) directly transmitted through the bare silica substrate without any analyzer. The cross-PCE of the metasurface is calculated as: $\left(\frac{1}{mn}\sum_{i,j}\frac{I_{p,q}^{o1/o2}}{I_{p,q}^{in1/in2}}\right)\times 100\%$.

Data availability

All data needed to evaluate the conclusions in the paper are present in the paper and/or the Supplementary Materials. Additional data related to this paper may be requested from the authors.

References

1. Forbes, A., de Oliveira, M. & Dennis, M. R. Structured light. *Nat. Photonics* **15**, 253–262 (2021).
2. Wang, J. & Liang, Y. Generation and detection of structured light: a review. *Front. Phys.* **9**, 688284 (2021).
3. He, C., Shen, Y. & Forbes, A. Towards higher-dimensional structured light. *Light. Sci. Appl.* **11**, 205 (2022).
4. Maurer, C., Jesacher, A., Fürhapter, S., Bernet, S. & Ritsch-Marte, M. Tailoring of arbitrary optical vector beams. *N. J. Phys.* **9**, 78–78 (2007).
5. Rosales-Guzmán, C., Ndagano, B. & Forbes, A. A review of complex vector light fields and their applications. *J. Opt.* **20**, 123001 (2018).
6. Li, P. et al. Generation of perfect vectorial vortex beams. *Opt. Lett.* **41**, 2205–2208 (2016).
7. Wan, Z., Wang, H., Liu, Q., Fu, X. & Shen, Y. Ultra-degree-of-freedom structured light for ultracapacity information carriers. *ACS Photonics* **10**, 2149–2164 (2023).
8. Yang, Y., Ren, Y.-X., Chen, M., Arita, Y. & Rosales-Guzmán, C. Optical trapping with structured light: a review. *Adv. Photonics* **3**, 034001 (2021).
9. Vaezi, M., Seitz, H. & Yang, S. A review on 3D micro-additive manufacturing technologies. *Int. J. Adv. Manuf. Technol.* **67**, 1721–1754 (2012).
10. Parigi, V. et al. Storage and retrieval of vector beams of light in a multiple-degree-of-freedom quantum memory. *Nat. Commun.* **6**, 7706 (2015).
11. Dong, M.-X. et al. Highly efficient storage of 25-dimensional photonic qudit in a cold-atom-based quantum memory. *Phys. Rev. Lett.* **131**, 240801 (2023).
12. Rodrigo, J. A., Alieva, T., Abramochkin, E. & Castro, I. Shaping of light beams along curves in three dimensions. *Opt. Express* **21**, 20544–20555 (2013).
13. He, M. et al. Generalized perfect optical vortices with free lens modulation. *Photonics Res.* **11**, 27–34 (2022).
14. Chang, C., Gao, Y., Xia, J., Nie, S. & Ding, J. Shaping of optical vector beams in three dimensions. *Opt. Lett.* **42**, 3884–3887 (2017).
15. Gu, T., Kim, H. J., Rivero-Baleine, C. & Hu, J. Reconfigurable metasurfaces towards commercial success. *Nat. Photonics* **17**, 48–58 (2022).
16. Kuznetsov, A. I. et al. Roadmap for optical metasurfaces. *ACS Photonics* **11**, 816–865 (2024).
17. Wang, H. et al. Coloured vortex beams with incoherent white light illumination. *Nat. Nanotechnol.* **18**, 264–272 (2023).
18. Ren, H. et al. Complex-amplitude metasurface-based orbital angular momentum holography in momentum space. *Nat. Nanotechnol.* **15**, 948–955 (2020).
19. Song, Q., Odeh, M., Zúñiga-Pérez, J., Kanté, B. & Genevet, P. Plasmonic topological metasurface by encircling an exceptional point. *Science* **373**, 1133–1137 (2021).
20. Choi, E. et al. 360° structured light with learned metasurfaces. *Nat. Photonics* **18**, 848–855 (2024).
21. Zhang, F. et al. Meta-optics empowered vector visual cryptography for high security and rapid decryption. *Nat. Commun.* **14**, 1946 (2023).
22. Zhang, X. et al. Basis function approach for diffractive pattern generation with Dammann vortex metasurfaces. *Sci. Adv.* **8**, eabp8073 (2022).
23. Luo, X. et al. Vector optical field manipulation via structural functional materials: Tutorial. *J. Appl. Phys.* **131**, 181101 (2022).
24. Khorasaninejad, M. & Capasso, F. Metalenses: Versatile multifunctional photonic components. *Science* **358**, eaam8100 (2017).
25. Arbabi, A. & Faraon, A. Advances in optical metalenses. *Nat. Photonics* **17**, 16–25 (2022).
26. Li, L. et al. Single-shot deterministic complex amplitude imaging with a single-layer metalens. *Sci. Adv.* **10**, eadl0501 (2024).
27. Song, Q., Liu, X., Qiu, C.-W. & Genevet, P. Vectorial metasurface holography. *Appl. Phys. Rev.* **9**, 011311 (2022).
28. Dorrah, A. H. & Capasso, F. Tunable structured light with flat optics. *Science* **376**, eabi6860 (2022).
29. Wang, X. et al. Advances in information processing and biological imaging using flat optics. *Nat. Rev. Electr. Eng.* **1**, 391–411 (2024).
30. Zheng, H. et al. Multichannel meta-imagers for accelerating machine vision. *Nat. Nanotechnol.* **19**, 471–478 (2024).
31. Dorrah, A. H., Rubin, N. A., Zaidi, A., Tamagnone, M. & Capasso, F. Metasurface optics for on-demand polarization transformations along the optical path. *Nat. Photonics* **15**, 287–296 (2021).
32. Dorrah, A. H., Rubin, N. A., Tamagnone, M., Zaidi, A. & Capasso, F. Structuring total angular momentum of light along the propagation direction with polarization-controlled meta-optics. *Nat. Commun.* **12**, 6249 (2021).
33. Li, Y. et al. Longitudinally variable 3D optical polarization structures. *Sci. Adv.* **9**, eadj6675 (2023).
34. Bao, Y., Ni, J. & Qiu, C. W. A minimalist single-layer metasurface for arbitrary and full control of vector vortex beams. *Adv. Mater.* **32**, 1905659 (2019).
35. Liu, M. et al. Broadband generation of perfect Poincaré beams via dielectric spin-multiplexed metasurface. *Nat. Commun.* **12**, 2230 (2021).
36. Ahmed, H. et al. Dynamic control of hybrid grafted perfect vector vortex beams. *Nat. Commun.* **14**, 3915 (2023).
37. Chen, J. et al. Phase-encoding truncated orbital angular momentum modes for high-security and high-capacity information encryption. *J. Lightwave Technol.* **42**, 3677–3683 (2024).
38. Kumar, P., Nishchal, N. K. & AlFalou, A. Controllable optical vortex array for image encoding. *IEEE Photonics Technol. Lett.* **34**, 521–524 (2022).
39. Baliyan, M. & Nishchal, N. K. Optical cryptography with C-point vector beams. *Opt. Lasers Eng.* **180**, 108337 (2024).
40. Rodrigo, J. A. & Alieva, T. Freestyle 3D laser traps: tools for studying light-driven particle dynamics and beyond. *Optica* **2**, 812–815 (2015).

Acknowledgements

This work is supported by Key Research and Development Program from Ministry of Science and Technology of China (2022YFA1205000 to T.X., 2023YFB2805800 to M.L. and 2022YFA1405000 to Y.L.), National Natural Science Foundation of China (12274217 to T.X., 62305152 to M.L., 62322507 to M.S.), the Natural Science Foundation of Jiangsu Province (BK20230780 to M.L., BK20220068 to T.X.), China Postdoctoral Science Foundation (2022M721550 to M.L.), Jiangsu Funding Program for Excellent Postdoctoral Talent (2023ZB196 to M. L.), and Fundamental Research Funds for the Central Universities. The authors acknowledge the technique support from the microfabrication center of the National Laboratory of Solid-State Microstructures.

Author contributions

M.L., Y.L., and T.X. conceived the idea. Y.L. and T.X supervised the project. M.L., and P.H. conducted the theoretical analysis. M.L. performed numerical simulations. M.L., and P.L. designed and fabricated the metasurface samples. M.L. performed the measurements and visualization with the help from H.Q. and R.J.. M.L., Y.L., and T.X. wrote the original draft. R.J., H.Z., Y.R. and M.S. provided useful discussions and comments. All the authors approved the manuscript.

Competing interests

The authors declare no competing interests.

Additional information

Supplementary information The online version contains supplementary material available at https://doi.org/10.1038/s41467-025-59234-y.

Correspondence and requests for materials should be addressed to Pengcheng Huo, Yan-qing Lu or Ting Xu.